

Contrast Enhancement of Echo Atom Interferometers using Optical Channeling and Optimization of Near Resonant Bragg Scattering

G. Carlse, J. Randhawa, E. Ramos, T. Vacheresse, A. Pouliot, and A. Kumarakrishnan*

Department of Physics and Astronomy, York University, Toronto, Ontario, Canada M3J 1P3

ABSTRACT

We investigate channeling oscillations in the contrast of a density grating formed by exposing a sample of ultracold atoms to an optical standing-wave pulse. We show that these dynamics can be imprinted on the free-induction decay signal following standing wave excitation as well as on the echo signal associated with a two-pulse atom interferometer (Carlse et al. Phys. Rev. A, 109, 043307 (2024)). Experimental results are supported by a simple model, which describes the grating contrast as the combination of two separate physical effects, namely, matter-wave interference and classical optical channeling resulting in Pendellösung-like oscillations. We also investigate the characteristics of near resonant Bragg scattering (Carlse et al. Phys. Rev. A. 110, 043306 (2024)), the underlying process that produces the echo signal. We explore how the density modulation produced in an atomic sample by momentum state interference and optical channeling can be optimally read out using a coherently Bragg-scattered traveling-wave electric field. When both the channeling and Bragg scattering processes are optimized, we report a 20-fold increase in scattering efficiency.

Keywords: Atom Interferometry, Precision Metrology, Laser Cooling and Trapping of Neutral Atoms, Atom Optics, Inertial Effects, Gravimeters, Coherent Transient Effects, Bragg Scattering

1. INTRODUCTION

Raman atom interferometers (AIs) have evolved into quantum sensors of choice for precision measurements of inertial effects [1–5] and for tests of fundamental principles [6–8]. They have also been developed for use in state-of-the-art portable sensors [9–15]. The focus on developing Raman AIs has overshadowed the potential of the single-state echo-type AI [16–20], a simpler experimental configuration that has achieved measurements of h/m and gravitational acceleration (g) with a sensitivity that is an order of magnitude lower than Raman AIs. Unlike Raman AIs, which manipulate laser cooled atoms between hyperfine ground states, grating-echo AIs rely on the interference of atoms with different momentum states associated with the same atomic ground state at specific echo times characterized by the cancellation of Doppler phases of momentum states. Accordingly, the grating-echo AI requires only one laser system, and it can avoid the need for velocity selection. By virtue of their simplicity, single-state echo AIs also have the potential to limit systematic effects due to level shifts arising from electric and magnetic fields. As a result, they offer promising alternatives techniques for precision measurements and inertial sensing.

While Raman AIs and related techniques achieve large momentum transfer to the atomic sample and scatter several thousand photons per atom during the detection stage of matter-wave interference, the signal strength for echo AIs, which depends on coherent scattering from a density grating, is limited to ~ 1 photon per atom. Previous work based on echo AIs has been further limited by the small contrast of density gratings. Therefore, to bridge this gap in sensitivity with respect to Raman AIs, it is necessary to understand the size of the grating contrast and investigate how it can be increased.

In the simplest version of the grating-echo AI, two standing wave (SW) pulses, separated by a time T , illuminate a laser cooled sample. This interaction produces momentum states separated by $2\hbar k$, where $k = 2\pi/\lambda$ is the wave vector and λ is the wavelength of light. Due to matter-wave interference, the momentum states evolve into a density grating after each excitation pulse. The grating formed after the first SW pulse is rephased in the vicinity of the echo time $t = 2T$ in a manner reminiscent of a photon echo[21], which is a well-known technique for canceling the effect of the velocity distribution of the sample. Unlike a typical photon echo experiment involving a relatively short-lived excited state, the grating-echo AI relies on a rephased ground-state density grating that can be probed by a coherently backscattered readout pulse.

Figure 1(a) shows a schematic diagram of the backscattered signal. Here, the readout pulse can be applied following either of the two excitation pulses or in the vicinity of the echo time. If the excitation pulses are short enough to satisfy the Raman-Nath criterion ($\tau < \tau_{RN}$, where τ_{RN} is the limit of the Raman-Nath regime), the momentum-state interference that produces the echo signal can be modeled using Kaptiza-Dirac diffraction of plane waves, an effect that was first demonstrated for atoms in Ref. [22].

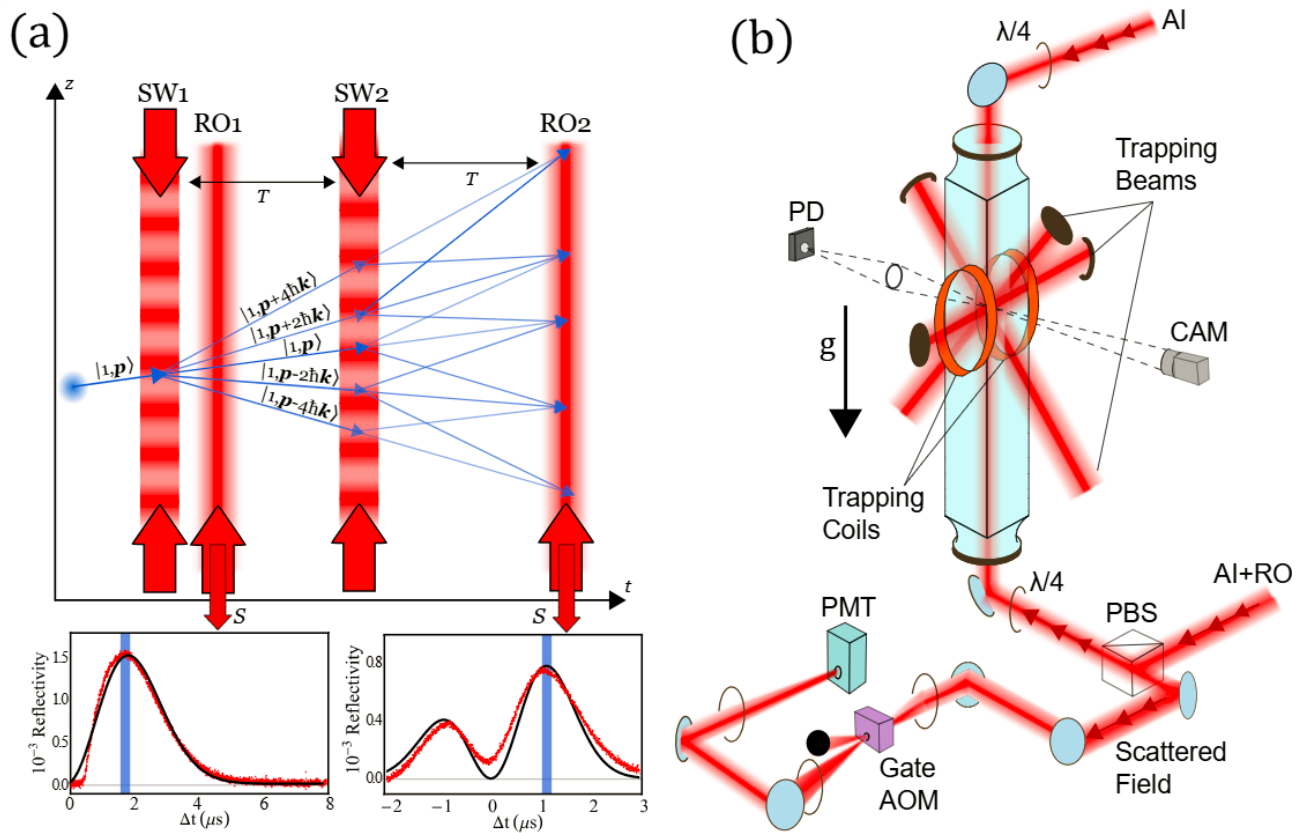


Figure 1. (a) Schematic of a grating-echo AI [33] involving standing wave excitation of a cold sample. Diffraction of a generic ground state $|1, \mathbf{p}\rangle$ is shown after both SW pulses. Also shown is the backscattered field (S) from a traveling-wave readout (RO) pulse applied immediately after the first SW pulse and at the echo time ($t = 2T$). The lower panels show signals (red points) and theoretical calculations (solid black lines) for a $\sim 10 \mu\text{K}$ sample of ^{85}Rb atoms in both one-pulse Free Induction Decay (FID) and echo configurations. Both panels show a vertical rectangular bar denoting the integration window used to measure the peak reflectivity of gratings. (b) Sketch of pyrex trapping cell and experimental setup, which uses an PMT gated by an AOM and an electronic gate for signal collection. The direction of g (along z) is shown with a downward arrow. Open circles represent lenses and closed circles, mirrors. CAM is a CCD camera, PD is trap fluorescence monitoring photodiode, PBS is polarizing cube beam splitter, and $\lambda/4$ is a quarter wave plate.

Previous calculations have modeled the contrast of the rephased density gratings in the Raman-Nath regime [16,17,20,23], assuming the diffraction of atomic plane waves and by averaging over the velocity distribution. These analytical calculations and numerical simulations can determine the density modulation of the wave function. While this approach successfully models signal shapes in the Raman-Nath limit, it provides an incomplete picture if the duration of the excitation pulses increases. In this intermediate regime, as well as in the well-studied long-pulse (Bragg) regime [24–27], there are two physical effects that contribute to the signal, namely, single-atom momentum-state interference, and the channeling of atoms at the nodes of the SW potential [28]. Characteristic channeling oscillations have been observed in demonstrations of Bragg scattering with cold atoms [27,29] as well as in experiments with Bose-Einstein condensates (BECs) [30]. In the intermediate regime, previous work has established a smooth transition between the Raman-Nath and Bragg regimes [27]. However, the enhanced contrast associated with channeling due to suitably long SW pulses has not been quantified in echo AI experiments. Related work with echo AIs, Ref. [31] has investigated signal

shapes by varying pulse parameters, while Ref. [32] investigated an alternative technique for increasing the grating contrast by loading the cold sample into a lattice during the trapping phase.

In this paper, we describe a complementary technique that relies on intermediate-length SW pulses that produce Pendellösung-like channeling oscillations in the contrast of the density grating [33]. We study the features of these oscillations by probing the grating contrast and recording the free-induction decay (FID) resulting from excitation by a single SW pulse. Here, the decay of the grating is governed by the time it takes a typical atom to move one period of the grating ($\lambda/2$). The dynamical contrast observed in the FID can then be imprinted on an echo signal in a two-pulse AI. In both configurations, we show the characteristic quadratic dependence of the signal on the SW pulse areas in the Raman-Nath regime and identify contrast enhancements attributable to channeling when this regime is violated using longer SW pulses. We explore how channeling can be used to increase the reflectivity of the sample in echo AI experiments. Our experimental results are supported by a simple model, that describes the contrast as the combination of two distinct physical effects: matter-wave interference and optical channeling in the classical sense, that result in Pendellösung-like oscillations.

In addition, we focus on a particularly striking feature of the one-pulse FID and two pulse echo AI experiments. In both experiments, the backscattered signal in response to the readout pulse results from coherent Bragg scattering from a phased array of dipole oscillators. The amplitude of these signals can be increased by increasing the contrast of the density modulation that characterizes the gratings. Furthermore, these signals exhibit a nonlinear dependence on the number of participating atoms and the detuning of the readout pulse from the ground-excited state resonance. While these features of coherent scattering have been explored in other optical crystals [35,36], they have not been investigated in the context of echo AI experiments.

In this paper, we also investigate how the Bragg reflectivity of a channeled grating-echo AI can be maximized. We measure the dependence of Bragg scattering on the detuning of the readout field, the number of atoms, and the degree of localization of atoms, which is controlled by the channeling effects of SW pulses. Our results [34] are supported with numerical simulations of classical channeling and Bragg scattering using a transfer matrix formalism [26,36]. We interpret our results on the basis of these simulations, which predict the expected enhancement in grating reflectivity over an extended range of channeling times and readout detunings. We demonstrate a 20-fold improvement in reflectivity in one-pulse FID experiments by optimizing both channeling and Bragg scattering processes [33, 34]. We demonstrate a similar improvement in a two-pulse grating-echo AI experiment. The enhanced reflectivity of gratings in echo AI experiments has renewed the possibility of extending the timescale of such experiments to improve sensitivity.

2. EXPERIMENTAL SETUP

The experimental setup resembles the apparatus described in Ref. [37] and is shown schematically in Fig. 1(b). A pyrex cell (~ 1 m in length) with rectangular faces and a square cross section contains room-temperature rubidium vapor. The system is pumped with an ion pump located ~ 1 m below the cell. The chamber contains a locally heated Rb source. Under typical operating conditions, the background pressure is $\sim 10^{-9}$ Torr and the trap loading time is ~ 5 s. The trapping, repump, and AI beams are derived using master-oscillator power-amplifier (MOPA) systems consisting of tapered amplifiers seeded with external cavity diode lasers [38,39]. The lasers are amplitude modulated by acousto-optic modulators (AOMs). After turning off the confining magnetic field gradient, the atoms from the magneto-optical-trap (MOT) are held in a molasses for 5.5 ms, while the trapping beams are detuned from -15 MHz to ~ -55 MHz to reduce heating. The vapor cell loaded MOT contains $\sim 10^9$ ^{85}Rb atoms at a temperature of ~ 10 μK . The temperature of the sample is determined by imaging the free expansion of the cloud using a CCD camera [40].

The size of the MOT, determined by the CCD camera and the number of atoms, N , determined by a MOT fluorescence monitoring photodiode [23,37,40] are varied by changing the repetition rate of the experiment, the intensity of the repump light, and the magnetic field gradient of the MOT coils. The AI excitation is composed of two circularly polarized ($\sigma^+ - \sigma^+$) counterpropagating pulses directed along the vertical. To reduce the effect of spontaneous emission during the excitation, these traveling wave components of the SW excitation are typically tuned ≈ 390 MHz above ν_0 , the $F = 3 \rightarrow F = 4$ transition in ^{85}Rb . This is accomplished using a frequency shifting 125 MHz acousto-optic modulator (AOM) operated in dual-pass configuration [41,42] which also reduces background leakage light. These SW excitation pulses, which are applied after the MOT has been released from the optical molasses, can be used to control channeling as described in Ref. [33].

In order to study near-resonant Bragg scattering produced by the readout field, we tune this pulse over a range of $\nu_0 \pm 50$ MHz using separate AOM chains (Arm 1 and Arm 2 in Fig. 2). To facilitate the desired tuning range, after the MOT is turned off, we generate the readout pulse from the same MOPA system used to drive the trapping beams. Fig 2 shows the relevant beam paths and frequency shifts.

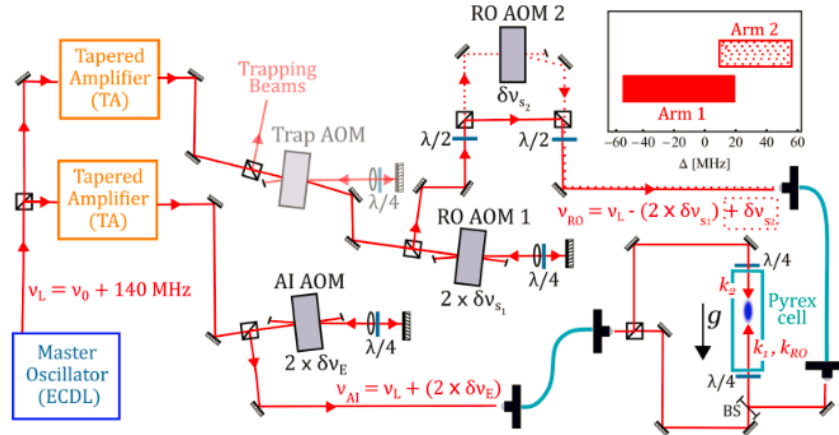


Figure 2. Schematic of the frequency shifts for AI and RO pulses used to investigate Bragg scattering [33]. The AI SW beams are generated from a dual-pass AOM (AI AOM, $\delta\nu_E = 125$ MHz) resulting in a detuning of ≈ 390 MHz. The RO is derived from the undiffracted beam of the trapping AOM. The RO is downshifted by a separate dual-pass AOM (RO AOM 1), shown by the solid beam path, in Arm 1. The resulting frequency shift is $2\delta\nu_{s1}$ where $\delta\nu_{s1}$ ranges from -60 MHz to -95 MHz. For additional tuning range, the output of RO AOM 1 can be directed into a single pass AOM (RO AOM 2), which produces an additional frequency shift of $\delta\nu_{s2}$ that ranges between 70 MHz and 90 MHz. This beam path, (Arm 2), is indicated by the dashed line. The full tuning range of the RO using both arms is shown as an inset. All detunings are with respect to the $F = 3 \rightarrow F' = 4'$ transition in ^{85}Rb (ν_0). The directions of the beams relative to the trapping chamber and g are also indicated. $\lambda/4$ is a quarter waveplate, $\lambda/2$ is a half waveplate, BS is a 50:50 nonpolarizing beamsplitter.

The AI SW beams are spatially overlapped with the readout beam using a 50:50 beamsplitter. All of these beams have nominal waists of ≈ 3 mm. In these experiments, the readout power is varied in the range of 1 – 10 mW, while the traveling wave components of SW pulses have powers of ≈ 10 mW. This excitation intensity corresponds to a single-beam Rabi frequency $\Omega_0 = 3\Gamma$, where Γ is the radiative rate of the excited state. As described in Refs. [33,34], the backscattered signals from the sample are collected using a photomultiplier tube gated both by an electronic circuit (rise time ≈ 200 ns) and by a 250 MHz AOM. The gating AOM has an optical efficiency of $\approx 20\%$ and a rise time of ≈ 100 ns. Signals are recorded with a digital oscilloscope with a bandwidth of 80 MHz. We measure the power of the readout beam using a calibrated photodiode and calculate the reflected fraction of the readout light from the sample. We assume that the scattered beam has the same spatial extent as the incident readout beam and determine the reflectivity as the ratio of the power in the incoming and reflected beams. We measure the peak reflectivity (R_{pk}) across the integration time window of the scattered field envelope as shown in Fig. 1(a), and report the average of four to eight repetitions.

3. RESULTS AND DISCUSSION

Figure 3(a) shows the peak reflectivity from the one-pulse FID experiment as a function of the SW pulse area within the Raman-Nath limit. As predicted by theory [33], we observe a distinct quadratic dependence for a small pulse area, independent of the atom-field coupling strength of the SW excitation ($\Omega_0^2/2\Delta$), where Δ is the detuning with respect to the excited state. Here we display data for pulse durations less than one fifth of the characteristic harmonic oscillator period $\tau_{HO} = (\pi^2\Delta/(\Omega_0^2\omega_q))^{1/2}$, where ω_q is the recoil frequency. In this regime, the atomic motion satisfies the Raman-Nath criterion. Figure 3(b) shows the peak reflectivity for the one-pulse FID experiment over a wider range of pulse areas that violate the Raman-Nath criterion. Based on the simple model presented in reference [33], the maximum reflectivity for a particular atom-field coupling corresponds to a distinct pulse area, in contrast to predictions that do not consider channeling. Comparing the largest signals [shown in Fig. 3(b)] with the maximum reflectivity observed within the

Raman-Nath limit [shown in Fig. 3(a)], we note that the reflectivity is enhanced by ~ 2.5 times when the Raman-Nath limit is violated. This enhancement can be attributed to atoms that are channeled to the nodes in the SW potential.

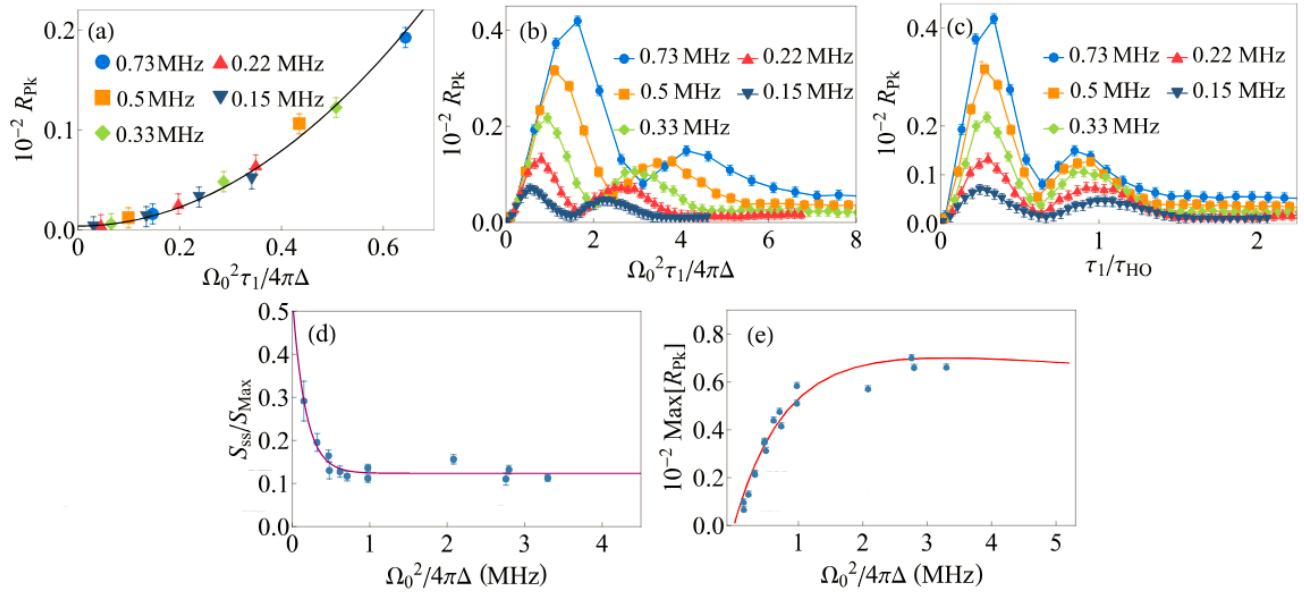


Figure 3. (a-c) Peak reflectivity (R_{pk}) measured in one-pulse FID experiment for a variety of atom-field coupling strengths ($\Omega_0^2/2\Delta$) (inset legends), (a) for small excitation pulse areas shows a quadratic dependence (black line), (b) for a larger range of pulse areas, and (c) as a function of the SW pulse length (plotted as a fraction of τ_{HO}). The data were obtained with an excitation detuning of $\Delta = 390$ MHz. (d) Ratio of steady-state and maximum reflectivities (indicated by the relative scattered field intensity, S) as a function of atom-field coupling with an exponential fit to the data (solid line). (e) Maximum peak reflectivity observed as a function of the atom-field coupling. Here the SW detuning was varied between $\Delta = 160$ MHz and $\Delta = 390$ MHz to further vary the atom-field coupling. The solid line shows the results of optical channeling simulations with $\tau_{RN} = 0.18 \tau_{HO}$. Adapted from reference [33].

Figure 3(c) shows the same data as Fig. 3(b), plotted as a function of the SW pulse width (τ_1), in units of τ_{HO} . Recasting the data in this manner synchronizes the Pendellösung-like oscillations in reflectivity, revealing the characteristic channeling period predicted by the model in reference [33]. This agreement suggests that when the Raman-Nath criterion is violated, the dominant contribution to the signal arises due to channeling of the sample in the potential. The trends in Fig. 3(c) suggest that the model in reference [33] is effective for understanding the data. However, a more elaborate model based on density variations in the sample and light propagation through the vapor may be required to understand features such as the absence of more than one revival in the reflectivity. In general, the oscillation period in a sinusoidal SW potential can be expected to deviate from τ_{HO} which is the prediction for a harmonic oscillator potential. These deviations were noted in Ref. [29] and observed in Ref. [30] by exposing a BEC to an optical potential with a small well depth. We note that rescaling the data as shown in Fig. 3(c) allows a direct visualization of the underlying channeling period for anharmonic potentials of varying depths. In the same manner, this rescaling also reveals the slight dephasing of subsequent oscillations of the reflectivity predicted by theory. This effect can be attributed to experimental sources of decoherence. Figure 3(d) shows the ratio of the steady-state reflectivity to the first maximum in the peak reflectivity as a function of the atom-field coupling strength. We find that this ratio scales inversely as the coupling strength is increased, a trend that is consistent with the model in reference [33].

Figure 3(e) shows the maximum peak reflectivity measured as a function of the atom-field coupling in the one-pulse FID experiment. The solid line shows the predictions of theory with an overall scale factor of $\alpha = 0.7$ and $\tau_{RN} = 0.18 \tau_{HO}$. While the agreement appears reasonable, this comparison demonstrates the sensitivity of the theoretical model to τ_{RN} , which is a free parameter. These data also suggest that the largest peak reflectivity is achieved with a modest atom-field coupling which optimizes both the momentum-state interference and the channeling effect. Therefore, a larger atom-field

coupling is not expected to further increase the reflectivity. Nevertheless, the first maximum in the peak reflectivity can still be exploited in echo experiments to increase the signal to noise ratio.

In Fig. 4 we show that the trends in Fig. 3 are replicated in two-pulse (echo AI) experiments when the width of the first SW pulse is varied. Comparing the maximum reflectivity [Fig. 4(b)] with the largest reflectivity attained in the Raman-Nath limit [Fig. 4(a)], we find an enhancement of ~ 2 times when the atoms are channeled with a first SW pulse, which is sufficiently long to violate the Raman-Nath criterion.

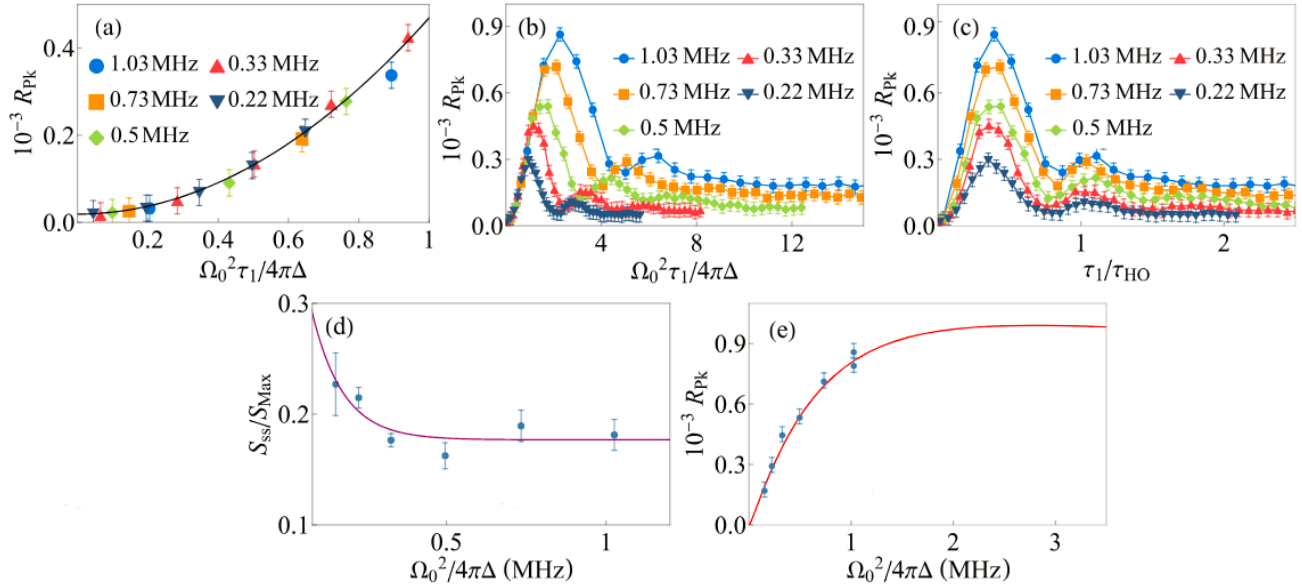


Figure 4. (a-c) R_{pk} measured in two-pulse grating-echo AI experiments for a variety of atom-field coupling strengths (inset legends), (a) for small excitation pulse areas showing a quadratic fit (black line), (b) for a larger range of first SW pulse areas, and (c) as a function of the first SW pulse length (as a fraction of τ_{HO}). (d) Ratio of steady-state and maximum reflectivities (indicated by the relative scattered field intensity, S) as a function of atom-field coupling with an exponential fit to the data (solid line). (e) Maximum R_{pk} for each atom-field coupling. The solid line shows the predictions of channeling simulation with $\tau_{RN} = 0.20 \tau_{HO}$ chosen to match the experimental data. Additional experimental parameters include pulse separation $T = 70.2 \mu s$, second pulse duration $\tau_2 \approx 0.15 \tau_{HO}$, and excitation detuning $\Delta = 390$ MHz. Adapted from reference [33].

Another feature of the echo experiment is that it is possible to further optimize sample reflectivity by varying the duration of the second SW excitation pulse (τ_2). Figure 5 shows the reflectivity in an echo experiment in which the second SW pulse width is varied, and the first excitation pulse width is fixed ($\tau_1 = 0.3 \tau_{HO}$) such that the corresponding one-pulse signal is maximized. Figure 5(a) shows the reflectivity as a function of the second SW pulse area, while Fig. 5(b) shows the same quantity as a function of the second SW pulse width in units of τ_{HO} . The solid vertical line in Fig. 5(b) defines the Raman-Nath criterion taken as $\tau_2 \approx 0.2 \tau_{HO}$, and the enhancement in reflectivity achieved by increasing the second SW pulse width beyond this limit. The reflectivity for various atom-field coupling strengths exhibits clear maxima that are in phase with respect to the pulse width (as a fraction of τ_{HO}), but not in terms of the pulse area, trends which are similar to those in Figs. 4(b) and 4(c). However, there are no prominent revivals in the reflectivity if the pulse width is further increased in these two pulse echo AI experiments. The enhancement in reflectivity resulting from the use of a second pulse which violates the Raman-Nath criterion has been investigated in Ref. [32] in the presence of a long ($\tau_1 \gg 100 \tau_{HO}$) lattice loading pulse that was applied when atoms were loaded into the MOT. Reference [32] reported an overall fourfold enhancement in reflectivity resulting from the non-Raman-Nath pulse after the confinement of atoms at the nodes of the SW lattice potential. As shown in Fig. 5(b), our results suggest that an approximately threefold enhancement is achieved by allowing the second excitation pulse to violate the Raman-Nath criterion, following a first pulse with $\tau_1 \approx 0.3 \tau_{HO}$, applied after the confining forces of the MOT are turned off.

Figure 6(a) shows the reflectivity spectra for the one-pulse FID signal as a function of the readout detuning. Here, representative calculations from a sequential density model described in reference [34] are shown as solid lines. We find that the scattering spectrum is well modeled by including the effect of channeling. Far from resonance, this behavior can be understood on the basis of a model that describes Bragg scattering from a phased array of dipoles. This model predicts a Lorentzian dependence for the reflectivity. As the detuning of the readout beam is reduced, the increase in atom-field coupling leads to enhanced scattering. However, near the excited state resonance, the sequential density model predicts a decrease in coherent scattering due to absorptive and multiple scattering effects, a feature prominent in the experimental data. As a result, it is possible to understand the two-peaked reflectivity spectrum.

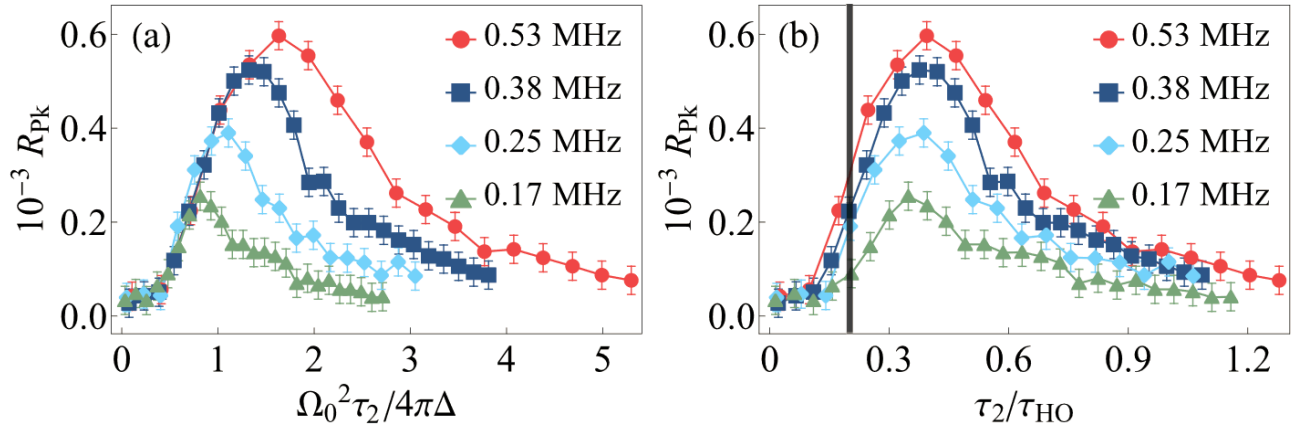


Figure 5. R_{pk} of grating-echo experiments as a function of the second pulse duration for a range of atom-field coupling strengths (inset legends). Results are plotted against (a) the pulse area and (b) the pulse duration as a fraction of τ_{HO} . The vertical bar in (b) shows the predicted limit of the Raman-Nath regime, taken as $\tau_2 \sim 0.2 \tau_{HO}$. Additional experimental parameters include pulse separation $T = 70.2 \mu s$, first SW pulse length $\tau_1 = 0.3 \tau_{HO}$, and excitation detuning of $\Delta = 160$ MHz. Adapted from [33].

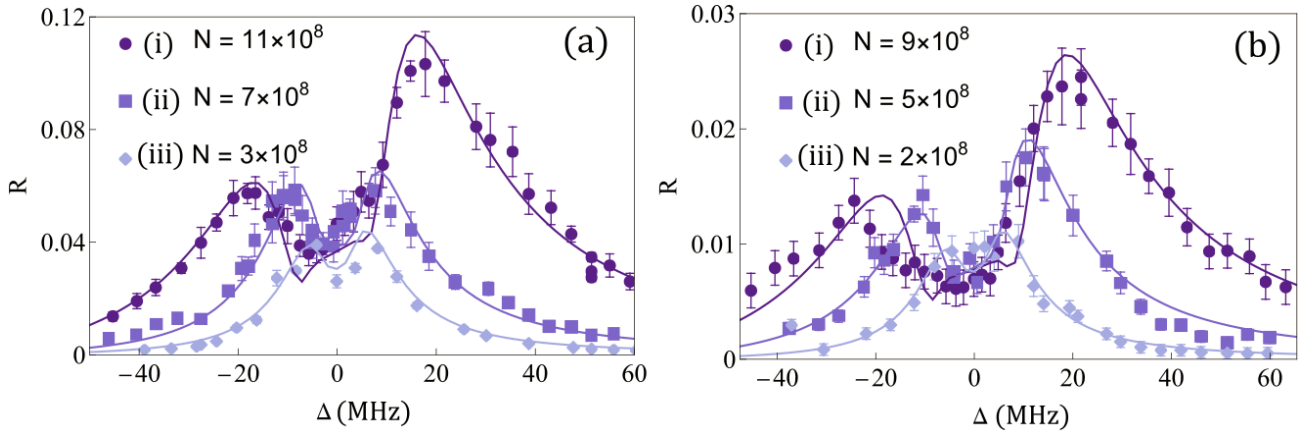


Figure 6. Reflectivity coefficient R for (a) the one-pulse FID and (b) the two-pulse grating-echo AI in samples containing different numbers of atoms (inset legends). Solid lines show fits based on theoretical calculations [34]. The SW excitation pulses have durations of $\tau \approx 0.3 \tau_{HO}$ and the occupation number parameters are (a): (i) $f_R = 0.57 \pm 0.03$, (ii) $f_R = 0.58 \pm 0.02$, and (iii) $f_R = 0.54 \pm 0.01$ and (b): (i) $f_R = 0.26 \pm 0.01$, (ii) $f_R = 0.26 \pm 0.02$, and (iii) $f_R = 0.27 \pm 0.04$. Adapted from reference [34].

Figure 6(b) shows the reflectivity spectra for the two-pulse grating-echo AI as a function of the readout detuning. Here, we note the similarity between the echo spectra and their FID counterparts shown in Fig. 6(a), including reduced reflectivity for small readout detunings in samples with more atoms. In general, we observe a comparable fourfold increase as in Fig 6(a) by changing the readout detuning from 50 MHz to the peak value (≈ 20 MHz). The agreement between experiment and simulations (solid lines in Fig. 6(b)) shows that the sequential density model is also successful in modeling the reflectivity spectra for the two-pulse grating-echo experiments.

Although the echo technique faithfully reproduces a density modulation at the echo time, the application of the second SW pulse is a nonselective process resulting in many closed interferometric paths differing by $2\hbar k$, only a subset of which contribute to the signal. This effect, along with velocity dispersion resulting in the spreading of the atomic wave packets, leads to an overall reduction in the contrast of the density modulation at the echo time in comparison with $t = 0$, in one-pulse FID experiments. This change is evident in the reduction in the f_r parameter in the sequential density model, which characterizes the effective occupation number of the lattice. Accordingly, we find the main difference between Figs. 6(a) and 6(b) is the value of f_r , which is reduced from ≈ 0.56 for the one-pulse FID to ≈ 0.26 for the grating-echo AI.

To demonstrate the interplay between Bragg scattering and optical channeling, we show reflectivity spectra for increasing channeling durations in Figs. 7(a) and 7(b), for the one-pulse FID and the two-pulse grating-echo AI experiments, respectively. The agreement between experiment and simulation across a wide range of channeling times, illustrates the effectiveness of the model for both AI configurations. The maximum reflectivity occurs when the channeling time is $\tau \approx 0.3 \tau_{HO}$ in both the one-pulse FID and the grating-echo AI.

We note that previous echo experiments [16-18], which did not employ channeling, resulted in reflected fractions of $\approx 0.1\%$ for readout detunings of ≈ 50 MHz. We find these values in agreement with our experimental data when the excitation frequency is tuned far off resonance and pulse lengths are restricted to satisfy the Raman-Nath regime [e.g. $\Delta_{RO} \approx 50$ MHz for $\tau = 0.05 \tau_{HO}$ as shown in Fig. 7(b)]. Our results indicate that we can improve the reflectivity by nearly a factor of 20 through the combination of optical channeling and near-resonant Bragg scattering [e.g. $\Delta_{RO} \approx 15$ MHz for $\tau = 0.33 \tau_{HO}$ in Fig. 7(b)].

For our best conditions, corresponding to the largest number of atoms loaded into the trap, we report a peak reflectivity of 2.5% [Fig. 6(b)] for the grating-echo AI, representing a twenty-fold increase over the best results from previous measurements [18-20]. These increases in signal-to-noise ratio [33,34] pave the way for grating-echo AI measurements with longer timescales, renewing the possibility of improving the sensitivity of this technique.

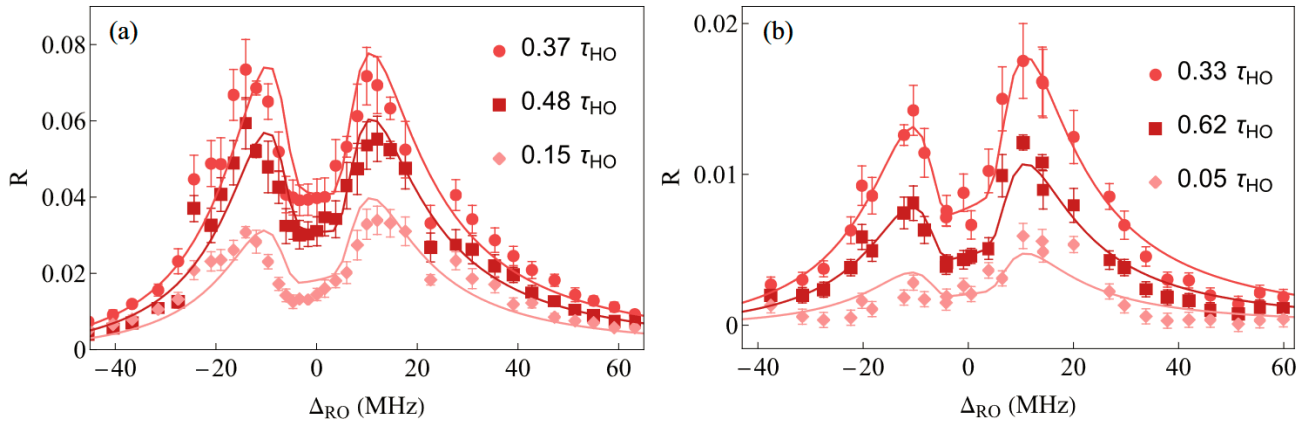


Figure 7. Reflection coefficient R , as a function of readout detuning resulting for different channeling times in (a) the one-pulse FID and (b) the two-pulse grating-echo AI. Solid lines show fits to theory for (a) $N = 7 \times 10^8$ with $f_r = 0.57 \pm 0.03$ and (b) $N = 6 \times 10^8$ with $f_r = 0.26 \pm 0.03$. Adapted from reference [34].

ACKNOWLEDGEMENTS

This work was supported by the Canada Foundation for Innovation, the Ontario Innovation Trust, the Ontario Centers of Excellence, the Natural Sciences and Engineering Research Council of Canada (NSERC), York University, and the Helen Freedhoff Memorial Fund. We also acknowledge helpful discussions with Louis Marmet of York University.

REFERENCES

- [1] Kasevich, M. and Chu, S., “Atomic interferometry using stimulated raman transitions,” *Phys. Rev. Lett.* 67, 181–184 (1991).
- [2] Peters, A., Chung, K. Y., and Chu, S., “Measurement of gravitational acceleration by dropping atoms,” *Nature* 400(6747), 849–852 (1999).
- [3] Snadden, M. J., McGuirk, J. M., Bouyer, P., Haritos, K. G., and Kasevich, M. A., “Measurement of the earth’s gravity gradient with an atom interferometer-based gravity gradiometer,” *Phys. Rev. Lett.* 81, 971–974 (1998).
- [4] McGuirk, J. M., Foster, G. T., Fixler, J. B., Snadden, M. J., and Kasevich, M. A., “Sensitive absolute-gravity gradiometry using atom interferometry,” *Phys. Rev. A* 65, 033608 (2002).
- [5] Hu, Z.-K., Sun, B.-L., Duan, X.-C., Zhou, M.-K., Chen, L.-L., Zhan, S., Zhang, Q.-Z., and Luo, J., “Demonstration of an ultrahigh-sensitivity atom-interferometry absolute gravimeter,” *Phys. Rev. A* 88, 043610 (2013).
- [6] Morel, L., Yao, Z., Cladé, P., and Guellati-Khélifa, S., “Determination of the fine-structure constant with an accuracy of 81 parts per trillion,” *Nature* 588(7836), 61–65 (2020).
- [7] Parker, R. H., Yu, C., Zhong, W., Estey, B., and Müller, H., “Measurement of the fine-structure constant as a test of the standard model,” *Science* 360(6385), 191–195 (2018).
- [8] Tino, G. M., Cacciapuoti, L., Capozziello, S., Lambiase, G., and Sorrentino, F., “Precision gravity tests and the Einstein equivalence principle,” *Progress in Particle and Nuclear Physics* 112, 103772 (2020).
- [9] Stray, B., Lamb, A., Kaushik, A., Vovrosh, J., Rodgers, A., Winch, J., Hayati, F., Boddice, D., Stabrawa, A., Niggebaum, A., et al., “Quantum sensing for gravity cartography,” *Nature* 602(7898), 590–594 (2022).
- [10] Wu, X., Pagel, Z., Malek, B. S., Nguyen, T. H., Zi, F., Scheirer, D. S., and Müller, H., “Gravity surveys using a mobile atom interferometer,” *Science Advances* 5(9), eaax0800 (2019).
- [11] López-Vázquez, A., Maldonado, M. A., Gomez, E., Corzo, N. V., de Carlos-López, E., ne, J. A. F. V., Jiménez-García, K., Jiménez-Mier, J., López-González, J. L., López-Monjaraz, C. J., López-Romero, J. M., Herrera, A. M., Méndez-Fragoso, R., Ortiz, C. A., na, H. P., no Borbolla, J. G. R., Ramírez-Martínez, F., and Valenzuela, V. M., “Compact laser modulation system for a transportable atomic gravimeter,” *Opt. Express* 31, 3504–3519 (2023).
- [12] Battelier, B., Barrett, B., Fouché, L., Chichet, L., Antoni-Micollier, L., Porte, H., Napolitano, F., Lautier, J., Landragin, A., and Bouyer, P., “Development of compact cold-atom sensors for inertial navigation,” in [Quantum Optics], Stuhler, J. and Shields, A. J., eds., 9900, 990004, International Society for Optics and Photonics, SPIE (2016).
- [13] Bidet, Y., Zahzam, N., Blanchard, C., Bonnin, A., Cadoret, M., Bresson, A., Rouxel, D., and Lequentrec-Lalancette, M., “Absolute marine gravimetry with matter-wave interferometry,” *Nature Communications* 9(1), 627 (2018).
- [14] Bidet, Y., Zahzam, N., Bresson, A., Blanchard, C., Cadoret, M., Olesen, A. V., and Forsberg, R., “Absolute airborne gravimetry with a cold atom sensor,” *Journal of Geodesy* 94, 1–9 (2020).
- [15] Freier, C., Hauth, M., Schkolnik, V., Leykauf, B., Schilling, M., Wziontek, H., Scherneck, H.-G., Müller, J., and Peters, A., “Mobile quantum gravity sensor with unprecedented stability,” *Journal of Physics: Conference Series* 723, 012050 (2016).
- [16] Cahn, S. B., Kumarakrishnan, A., Shim, U., Sleator, T., Berman, P. R., and Dubetsky, B., “Time-domain de broglie wave interferometry,” *Phys. Rev. Lett.* 79, 784–787 (1997).
- [17] Barrett, B., Chan, I., Mok, C., Carew, A., Yavin, I., Kumarakrishnan, A., Cahn, S. B., and Sleator, T., “Time-domain interferometry with laser-cooled atoms,” in [Advances in Atomic, Molecular, and Optical Physics], 60, 119–199, Elsevier (2011).
- [18] Barrett, B., Carew, A., Beattie, S., and Kumarakrishnan, A., “Measuring the atomic recoil frequency using a modified grating-echo atom interferometer,” *Phys. Rev. A* 87, 033626 (2013).
- [19] Mok, C., Barrett, B., Carew, A., Berthiaume, R., Beattie, S., and Kumarakrishnan, A., “Demonstration of improved sensitivity of echo interferometers to gravitational acceleration,” *Phys. Rev. A* 88, 023614 (2013).
- [20] Barrett, B., Carew, A., Beica, H. C., Vorozcovs, A., Pouliot, A., and Kumarakrishnan, A., “Prospects for precise measurements with echo atom interferometry,” *Atoms* 4(3), 19 (2016).
- [21] Abella, I. D., Kurnit, N. A., and Hartmann, S. R., “Photon echoes,” *Phys. Rev.* 141, 391–406 (1966).
- [22] Gould, P. L., Ruff, G. A., and Pritchard, D. E., “Diffraction of atoms by light: The near-resonant Kapitza-Dirac effect,” *Phys. Rev. Lett.* 56, 827–830 (1986).
- [23] Barrett, B., Techniques for measuring the atomic recoil frequency using a grating-echo atom interferometer,

Ph.D. thesis, York University (2012).

- [24] Martin, P. J., Gould, P. L., Oldaker, B. G., Miklich, A. H., and Pritchard, D. E., “Diffraction of atoms moving through a standing light wave,” *Phys. Rev. A* 36, 2495–2498 (1987).
- [25] Martin, P. J., Gould, P. L., Oldaker, B. G., Miklich, A. H., and Pritchard, D. E., “Diffraction of atoms from a standing light wave,” *Physica B+C* 151(1), 255–261 (1988).
- [26] Weidemüller, M., Hemmerich, A., Görlitz, A., Esslinger, T., and Hänsch, T. W., “Bragg diffraction in an atomic lattice bound by light,” *Phys. Rev. Lett.* 75, 4583–4586 (1995).
- [27] Deh, B., Marzok, C., Slama, S., Zimmermann, C., and Courteille, P. W., “Bragg spectroscopy and Ramsey interferometry with an ultracold Fermi gas,” *Applied Physics B* 97, 387–396 (2009).
- [28] Adams, C., Sigel, M., and Mlynek, J., “Atom optics,” *Physics Reports* 240(3), 143–210 (1994).
- [29] Dürr, S., Kunze, S., and Rempe, G., “Pendellösung oscillations in second-order Bragg scattering of atoms from a standing light wave,” *Quantum and Semiclassical Optics: Journal of the European Optical Society Part B* 8(3), 531 (1996).
- [30] Ovchinnikov, Y. B., Müller, J. H., Doery, M. R., Vredenburg, E. J. D., Helmerson, K., Rolston, S. L., and Phillips, W. D., “Diffraction of a released Bose-Einstein condensate by a pulsed standing light wave,” *Phys. Rev. Lett.* 83, 284–287 (1999).
- [31] Beattie, S., Barrett, B., Weel, M., Chan, I., Mok, C., Cahn, S. B., and Kumarakrishnan, A., “Influence of spontaneous emission on a single-state atom interferometer,” *Phys. Rev. A* 77, 013610 (2008).
- [32] Andersen, M. F. and Sleator, T., “Lattice interferometer for laser-cooled atoms,” *Phys. Rev. Lett.* 103, 070402 (2009).
- [33] Carlse, G., Randhawa, J., Ramos, E., Vacheresse, T., Pouliot, A., Carew, A. C., and Kumarakrishnan, A., “Role of optical channeling in contrast enhancement of echo interferometers,” *Phys. Rev. A* 109, 043307 (2024).
- [34] Carlse, G., Randhawa, J., Ramos, E., Vacheresse, T., Pouliot, A., Carew, A. C., Kumarakrishnan, A., and Barrett, B., “Optimization of Bragg scattering from atomic gratings for echo interferometry,” *Phys. Rev. A* 110, 043306 (2024).
- [35] Birkel, G., Gatzke, M., Deutsch, I. H., Rolston, S. L., and Phillips, W. D., “Bragg scattering from atoms in optical lattices,” *Phys. Rev. Lett.* 75, 2823–2826 (1995).
- [36] Slama, S., von Cube, C., Kohler, M., Zimmermann, C., and Courteille, P. W., “Multiple reflections and diffuse scattering in Bragg scattering at optical lattices,” *Phys. Rev. A* 73, 023424 (2006).
- [37] Carlse, G., Pouliot, A., Vacheresse, T., Carew, A., Beica, H. C., Winter, S., and Kumarakrishnan, A., “Technique for magnetic moment reconstruction of laser-cooled atoms using direct imaging and prospects for measuring magnetic sublevel distributions,” *J. Opt. Soc. Am. B* 37, 1419–1427 (2020).
- [38] Beica, H. C., Pouliot, A., Carew, A., Vorozcovs, A., Afkhami-Jeddi, N., Carlse, G., Dowling, P., Barron, B., and Kumarakrishnan, A., “Characterization and applications of auto-locked vacuum-sealed diode lasers for precision metrology,” *Rev. Sci. Instrum.* 90(8), 085113 (2019).
- [39] Pouliot, A., Beica, H. C., Carew, A., Vorozcovs, A., Carlse, G., Barrett, B., and Kumarakrishnan, A., “Investigations of optical pumping for magnetometry using an auto-locking laser system,” in [Laser Technology for Defense and Security XIV], Dubinskiy, M. and Newell, T. C., eds., 10637, 106370A, International Society for Optics and Photonics, SPIE (2018).
- [40] Vorozcovs, A., Weel, M., Beattie, S., Cauchi, S., and Kumarakrishnan, A., “Measurements of temperature scaling laws in an optically dense magneto-optical trap,” *J. Opt. Soc. Am. B* 22, 943–950 (2005).
- [41] Donley, E. A., Heavner, T. P., Levi, F., Tataw, M., and Jefferts, S. R., “Double-pass acousto-optic modulator system,” *Review of Scientific Instruments* 76(6) (2005).
- [42] Cauchi, S., Vorozcovs, A., Weel, M., Beattie, S., Gagnon, O., and Kumarakrishnan, A., “Absorption spectroscopy of trapped rubidium atoms,” *Canadian Journal of Physics* 82(11), 905–916 (2004)